J. Fluid Mech. (2013), *vol.* 714, *pp.* 591–611. © Cambridge University Press 2013
doi:10.1017/jfm.2012.507

Bottom-pressure observations of deep-sea internal hydrostatic and non-hydrostatic motions

Hans van Haren†

NIOZ Royal Netherlands Institute for Sea Research, PO Box 59,
1790 AB Den Burg, the Netherlands

(Received 23 February 2012; revised 8 October 2012; accepted 10 October 2012)

In the ocean, sloping bottom topography is important for the generation and dissipation of internal waves. Here, the transition of such waves to turbulence is demonstrated using an accurate bottom-pressure sensor that was moored with an acoustic Doppler current profiler and high-resolution thermistor string on the sloping side of the ocean guyot 'Great Meteor Seamount' (water depth 549 m). The site is dominated by the passage of strong frontal bores, moving upslope once or twice every tidal period, with a trail of high-frequency internal waves. The bore amplitude and precise timing of bore passage vary every tide. A bore induces mainly non-hydrostatic pressure, while the trailing waves induce mainly internal hydrostatic pressure. These separate (internal wave) pressure terms are independently estimated using current and temperature data, respectively. In the bottom-pressure time series, the passage of a bore is barely visible, but the trailing high-frequency internal waves are. A bore is obscured by higher-frequency pressure variations up to $\sim 4 \times 10^3$ cpd $\approx 80N$ (cpd, cycles per day; N, the large-scale buoyancy frequency). These motions dominate the turbulent state of internal tides above a sloping bottom. In contrast with previous bottom-pressure observations in other areas, infra-gravity surface waves contribute little to these pressure variations in the same frequency range. Here, such waves do not incur observed pressure. This is verified in a consistency test for large-Reynolds-number turbulence using high-resolution temperature data. The high-frequency quasi-turbulent internal motions are visible in detailed temperature and acoustic echo images, revealing a nearly permanently wave-turbulent tide going up and down the bottom slope. Over the entire observational period, the spectral slope and variance of bottom pressure are equivalent to internal hydrostatic pressure due to internal waves in the lower 100 m above the bottom, by non-hydrostatic pressure due to high-frequency internal waves and large-scale overturning. The observations suggest a transition between large-scale internal waves, small-scale internal tidal waves residing on thin ($\sim$1 m) stratified layers and turbulence.

Key words: geophysical and geological flows, mixing and dispersion, ocean processes

---

† Email address for correspondence: hans.van.haren@nioz.nl

1. Introduction

1.1. *Internal waves in the ocean*

The vertically density-stratified open ocean is constantly in motion, thereby moving interfaces, $O(1–10\ \mathrm{m})$ in thickness, coherently up and down over vertical distances $O(10–100\ \mathrm{m})$ (see e.g. Pinkel 1981; van Haren & Gostiaux 2009). These ubiquitous 'inertia-gravity' waves (IWs) can propagate freely in all three (x, y, z) spatial dimensions when their frequencies (σ) are in the range $f \leqslant \sigma \leqslant N$ when $N \gg f$, with f being the inertial frequency and N the buoyancy frequency. (When $N = O(f)$, these frequency bounds deviate substantially to frequencies below f and above N; see e.g. LeBlond & Mysak (1978) and, for a review, Gerkema *et al.* (2008).) Underwater topography such as a seamount acts as a source and a sink for them. The sloping bottom transfers the more or less linear waves from the interior into nonlinear waves up to spectacular frontal bores or solitary waves of elevation that extend up to 50 m above it (Klymak & Moum 2003; Hosegood & van Haren 2004). Such 'waves' occur at the periodicity of the dominant low-frequency carrier wave, but their frontal passages have a much shorter time scale, which is shorter than the buoyancy period.

In tidally dominated areas, this transfer from linear to nonlinear bore-like internal waves is generally thought to occur where the bottom slope (α) 'critically' matches the internal tide angle ($\beta = \sin^{-1}[(\sigma^2 - f^2)^{1/2} / (N^2 - f^2)^{1/2}]$, e.g. for semidiurnal lunar tidal $\sigma = M_2$). When $\alpha = \beta$, a concentration of energy (dissipation) is expected as IWs preserve their angle to the vertical (gravity) upon reflection; see recent modelling, (e.g. Slinn & Riley 1996; Gayen & Sarkar 2010). In the ocean, however, bore-like nonlinear waves have also been observed at 'non-critical slopes', i.e. slopes significantly different from critical (e.g. Bonnin *et al.* 2006; present data).

The precise mechanism of generation of such bores is still unknown. They could be the result of sloshing of a carrier wave, becoming unstable during its downslope phase, resulting in an upslope moving quasi-gravity current (Venayagamoorthy & Fringer 2007). Alternatively, they could be the manifestation of nonlinear waves of depression in the interior, possibly following interaction of internal (tidal) waves generated at topography nearby. Such interior nonlinear waves of depression become bore-like waves of elevation upon shoaling at topography (Vlasenko & Hutter 2002; Aghsaee, Boegman & Lamb 2010).

Laboratory work (e.g. Grue *et al.* 2000; Fructus *et al.* 2009) and numerical modelling (e.g. Slinn & Riley 1996; Lamb 2003; Xing & Davies 2006; Venayagamoorthy & Fringer 2007; Lamb & Farmer 2011) have demonstrated that nonlinear bores and solitary waves produce substantial turbulence, with trapped cores and strong vertical motions, followed by a trail of high-frequency internal waves and restratification. Turbulence in stratified waters is partially due to shear-induced Kelvin–Helmholtz instabilities, which grow up to 10 m amplitude above deep-sea topography (van Haren & Gostiaux 2010). However, these instabilities contribute only about 10 % of the turbulent mixing in the lower 50 m above a sloping bottom. The largest turbulence is produced by collapse of stratification, convective instability, prior to the bore-like front, and in the front itself (van Haren & Gostiaux 2012*a*). As stated by Slinn & Riley (1996), the internal wave field in the interior actively restratifies the near-bottom 'boundary layer'. Thus, near-bottom mixing is effective.

In order to learn more about effects in the ocean interior, we need further knowledge about the transition of wave energy to turbulent mixing and its efficiency above sloping bottoms in the deep ocean. There are several ways to investigate this, one of the more challenging being the use of the variable that directly represents dynamics, i.e. *in situ* bottom pressure. Here we explore data from an accurate pressure sensor moored on a bottom lander for a fortnight in a large-Reynolds-number and stratified ocean environment. To help interpret this signal, secondary observations are moored acoustic current meter data and high-resolution temperature data. These secondary observations can be used to estimate different bottom-pressure terms independently. The data are sampled at rates between 0.2 and 1 Hz. Such sampling rates are adequate to resolve all internal wave scales and the larger, energetic turbulence overturning Ozmidov scales, but not the turbulence dissipation scales.

1.2. *Observing internal wave turbulence using bottom-pressure sensors*

Bottom pressure has not been used in the ocean as an observational means for internal wave turbulence studies, for obvious reasons of measuring a small dynamic pressure $O(10\text{–}100\ \mathrm{N\ m^{-2}})$ in a huge $O(10^7\ \mathrm{N\ m^{-2}})$ static pressure environment. In the atmosphere, this discrepancy between static and dynamic pressures is smaller, and studies of atmospheric boundary layers often involve bottom-pressure registrations (e.g. Shaw *et al.* 1990; Cuxart *et al.* 2002). As ocean dynamics are similar in many respects to atmosphere dynamics, much can be learned from interpretation of atmospheric bottom-pressure signals prior to performing the more difficult analysis of ocean bottom pressure.

A night-time stably density-stratified atmospheric boundary layer shows a mix of internal gravity waves and turbulence (Cuxart *et al.* 2002). Both kinetic energy and bottom pressure show an intermittent pattern, suggesting evidence of breaking internal waves or Kelvin–Helmholtz instabilities. These instabilities do not necessarily occur at the bottom. They may be found some distance above it. The spectral shapes, for kinetic energy and pressure variance, show a partial 'background' $-5/3$ fall-off rate with frequency. Some coherent sub-maxima presumably evidence the buoyancy frequency. In the more convectively turbulent day-time, these sub-maxima blend into the $-5/3$ background (Cuxart *et al.* 2002). In the time domain, bottom pressure shows a typical intermittently variable signal with fairly constant amplitude: large spikes are not observed (see also Shaw *et al.* 1990).

Shaw *et al.* (1990) compare vertical velocity and pressure observations in the turbulent boundary layer beneath a forest to establish various turbulence pressure terms using independent observables. They reasonably confirm the direct bottom-pressure observations by two-dimensional integration of the Poisson equation describing variation in turbulence pressure,

$$\frac{\partial^2 p'}{\partial x_i \partial x_i} = -\bar{\rho}\left[\frac{2\partial \overline{u_i}\partial u'_j}{\partial x_j \partial x_i} + \frac{\partial^2 u'_i u'_j}{\partial x_i \partial x_j} + \frac{g\partial \theta'}{\bar{T}\partial x_i}\delta_{iz}\right], \tag{1.1}$$

in which the subscripts $i, j = x, y, z$ denote several components of the stress tensor, p is pressure, ρ is density, θ is potential temperature, T is temperature, g is acceleration of gravity, the overbar represents averaging over time and the prime indicates fluctuations about the averages. Shaw *et al.*'s (1990) time series of pressure are dominated by variations at lower frequencies than those of vertical velocity (w). This is not surprising considering the effects of integration in computing pressure following (1.1). The magnitude and phase of the large-scale structures are reasonably estimated, but the phase of the small-scale features is not. A frontal passage is dominated by the first term on the right-hand side of (1.1), notably the term including w' in the advective (average) current direction. This confirms laboratory experiments by

Thomas & Bull (1983). Other terms are about half to one order of magnitude smaller (in variance). They are thus not necessarily negligible. This explains the lack of precise detailed (phase) relationships in comparing observed pressure and estimated pressure terms. Thus, when turbulence is dominantly present in the bottom boundary layer, the variance of observed and estimated pressure may match, but coherent phase will not.

In the observations of Shaw *et al.* (1990), the burst/sweep cycle of a frontal passage is signalled first in w with pressure lagging $O(10\ \mathrm{s})$ behind. Pressure first dips and then reaches relative overpressure during the frontal passage, as in turbulent coherent structure passages (Thomas & Bull 1983).

In the ocean, instead of internal wave turbulence studies, mostly seismic and surface wave research has been done using bottom-pressure recorders. This includes pressure studies on low-frequency surface waves, which have amplitudes of only $O(10\text{–}100\ \mathrm{N\ m^{-2}})$, equivalent to $O(10^{-3}\text{–}10^{-2}\ \mathrm{m})$ in surface elevation. Such waves are little attenuated with depth because of their long wavelength/large periods: surface ‘infra-gravity waves’ (IGWs) with periods between about 30 and 500 s (Webb 1998). It is unclear why these dispersive surface waves would fill such a broad spectral band of more than a decade in frequency. This band is also relatively flat in variance, thus partially resembling band-limited white noise before rolling off at turbulence scaling slopes.

At lower frequencies down to tidal harmonics, a typical ocean bottom-pressure spectrum adopts a σ^{-2} drop-off rate at more or less constant power per frequency irrespective of its source and with no apparent seasonal cycle (Filloux 1980). This frequency band is typically the IW continuum band (IWC). It may transfer energy to turbulence across its own natural high-frequency cut-off at the buoyancy frequency N (Filloux 1980; D’Asaro & Lien 2000*a*,*b*).

The spectrum of large turbulence overturning scales at frequencies just higher than those of the IWC stands out as a rather flat, spikeless, broadband signal over a decade or more, which covers the same range as that of surface IGWs. In the case when these overturnings are generated by internal waves, it seems appropriate to adopt this flat broad band and its high-frequency roll-off as the ‘internal wave turbulence’ (IWT) band. The shape of this turbulence part of the bottom p spectrum, which contains very high-frequency internal waves supported by thin stratified layers, is well defined for turbulent wall layers, but in the laboratory and for free stream pressure observations in homogeneous turbulent flows mainly (e.g. Willmarth 1975; Tsuji *et al.* 2007). For turbulent wall layers, the p spectrum is also rather flat, slightly bulging to an insignificant peak halfway before dropping off at rates of initially σ^{-1}, then $\sigma^{-3/2}$–σ^{-2} and finally rolling off at a rate steeper than σ^{-3}. This p-spectral part occupies about one-and-a-half decades in frequency.

At sea, so far only during sparse passages of nonlinear solitary waves of elevation on a continental shelf, a bottom-pressure signal has been verified with independent estimates of internal hydrostatic and non-hydrostatic pressure that characterize internal wave motions. Their monthly mean pressure was attributed to overwhelming surface waves having a decade larger variance than that of internal waves (Moum & Nash 2008). Such verification will be presented here too, specifically aiming at the transition between internal waves and turbulence above a sloping deep-ocean bottom.

2. Computing bottom-pressure estimates

Apart from the analysis by Moum & Nash (2008), few attempts have been made to resolve dynamic parameters such as non-hydrostatic pressure (due to vertical velocity accelerations; p_{nh}) and internal hydrostatic pressure (baroclinic; p_{ih}) at the ocean bottom. Following Moum & Smyth (2006) the (non)linear internal wave pressure variations observed at level z just above the bottom and in the IWC (after subtraction of large-scale tidal variations) read

$$p'(-H+z,t)=p_{nh}+p_{ih}+p_{eh}=p_{obs}^{-H}, \tag{2.1a}$$

$$p_{nh}=\int_{z-H}^{0}\langle\rho\rangle\frac{\mathrm{D}w}{\mathrm{D}t}\,\mathrm{d}\tilde{z},\quad p_{ih}=\int_{z-H}^{0}\rho' g\,\mathrm{d}\tilde{z},\quad p_{eh}=\langle\rho\rangle g\eta, \tag{2.1b}$$

in which p_{eh} denotes the wave's external hydrostatic pressure at the sea surface, p_{obs}^{-H} is the observed (near) bottom pressure, H is water depth, η is wave-induced sea level variation and $\langle\ \rangle$ indicates a particular time average.

In $H = 70$–110 m on a continental shelf (Moum & Nash 2008), nonlinear internal waves induce predominantly $|p_{ih}| \gg |p_{nh}|, |p_{eh}|$. A solitary wave of depression generates a negative value in p_{ih} and positive values for the weaker terms. Typical values are $\sim$200 N m^{-2} for p_{nh} and up to 700 N m^{-2} for p_{ih} and p_{obs}^{-H}. These values are an order of magnitude larger than the ones to be presented here, which are from 5–8 times greater depths and are in part more representative of strongly non-hydrostatic 'wave' motions.

For near-bottom elevation waves far from the surface, wave-induced pressure terms $|p_{eh}| \ll |p_{nh}|, |p_{ih}|$, so that such waves are barely visible by radar or other surface measurement techniques (Moum & Smyth 2006). Their ratio of non-hydrostatic over hydrostatic pressure at the sea floor is expected to reduce to

$$R_{p,-H}\approx |p_{nh}|/|p_{ih}|. \tag{2.2}$$

Independently, sea-floor pressure can be obtained by integrating the near-bottom horizontal momentum equations,

$$p_{\mathrm{D}u/\mathrm{D}t}(-H+z,t)=-\langle\rho\rangle\int_{-\infty}^{x}\frac{\mathrm{D}u(-H+z,t)}{\mathrm{D}t}\,\mathrm{d}\tilde{x}\approx\langle\rho\rangle\int_{u(-H+z,t-t_0)}^{u(-H+z,t)}c\,\mathrm{d}\tilde{u}, \tag{2.3a}$$

$$p_{\mathrm{D}v/\mathrm{D}t}(-H+z,t)=-\langle\rho\rangle\int_{-\infty}^{x}\frac{\mathrm{D}v(-H+z,t)}{\mathrm{D}t}\,\mathrm{d}\tilde{x}\approx\langle\rho\rangle\int_{v(-H+z,t-t_0)}^{v(-H+z,t)}c\,\mathrm{d}\tilde{v}, \tag{2.3b}$$

in which c denotes the wave's phase speed. The transfer from horizontal coordinate to current integral assumes wave propagation without change of form. In practice, integration starts at some arbitrary $t_0 = 500$ s before wave arrival (Moum & Smyth 2006). Moum & Smyth (2006) find $p_{\mathrm{D}u/\mathrm{D}t} \approx 0.55(p_{ih}+p_{nh}+p_{eh})$ in the direction of wave propagation. The 0.55 factor smaller than unity they attribute to near-bottom turbulence terms not accounted for, as (2.3) reads, in more complete form,

$$p_{\mathrm{D}u/\mathrm{D}t}(-H+z,t)\approx\langle\rho\rangle\int_{u(-H+z,t-t_0)}^{u(-H+z,t)}c\,\mathrm{d}\tilde{u}+\int_{-\infty}^{x}\left.\frac{\partial\boldsymbol{\tau}}{\partial z}\right|_{-H}, \tag{2.4}$$

and similarly for $P_{\mathrm{D}v/\mathrm{D}t}$, in which $\boldsymbol{\tau}$ denotes the stress tensor. Likewise, one can add turbulence tensor terms to the vertical momentum equation, so that (2.1) becomes

$$p_{obs}^{-H}=p_{nh}+p_{ih}+p_{eh}-\int_{z-H}^{0}\nabla_i\cdot\boldsymbol{\tau}_{iz}\,\mathrm{d}\tilde{z}. \tag{2.5}$$

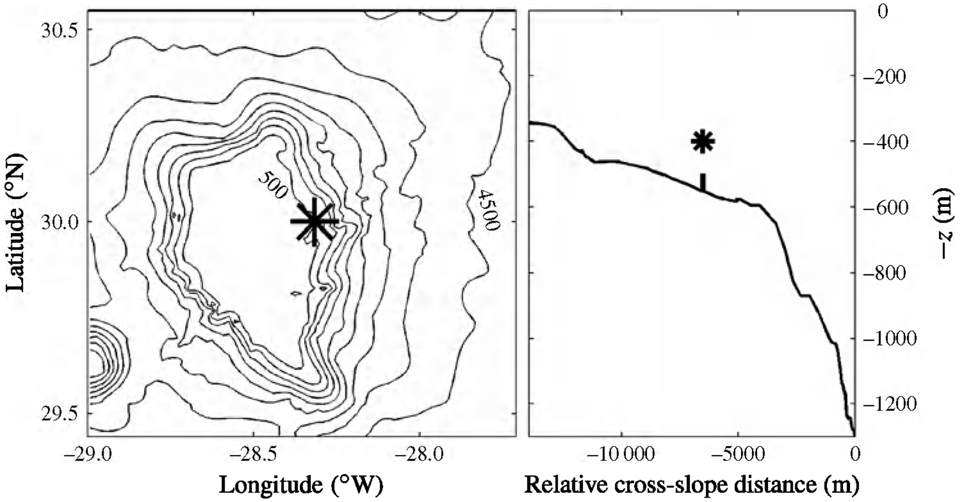

FIGURE 1. Location of mooring ($*$) near the top of Great Meteor Seamount. Bathymetry is computed from 1′ topography, an update from Smith & Sandwell (1997). Depth contour lines are every 500 m for [500, 4500] m. Above the east–west directed slope, thermistor string extent (vertical bar) and upper acoustic current meter ($*$) are indicated.

The reason for adding stress tensor terms is that, above sloping topography, turbulent overturning is expected besides highly nonlinear internal waves. Unfortunately, resolution of all terms in (2.4) and (2.5), including establishment of precise phase relationships, requires more instrumentation than presently employed. However, as will be reasoned in § 3, and as partially has been done above, the magnitudes of different pressure terms can be established with the present set-up to within a factor of 2 for internal waves and for the larger turbulent overturns. Following the atmospheric observations described in § 1.2, it is not expected to establish phase relationships between different pressure estimates that are mainly due to turbulence, commensurate with its (still unknown) three-dimensional character.

3. Data

Great Meteor Seamount (GMS) rises up to 300 m from the surface in an otherwise relatively flat, 5000 m deep Canary Basin in the North-East Atlantic Ocean. The dominant driving force of motions in this part of the ocean is the semidiurnal tide. About 250 m below GMS's summit, a 3 m × 2 m × 1.7 m sturdy bottom lander was moored at 549 m for 18 days in May–June 2006 (figure 1; see table 1 for mooring details). The mooring is well above the depth range of Mediterranean outflow and therefore temperature is an adequate tracer for density variations, with a tight relationship $\delta\rho = (-0.101 \pm 0.002)\delta T$ kg m^{-3} °C^{-1} as established from multiple conductivity–temperature–depth (CTD) casts in the vicinity of the mooring.

A deep-water SBE53 bottom-pressure recorder was mounted inside the lander, attached to its central axis. The recorder is equipped with a Digiquartz crystal, temperature-compensated pressure sensor that has an absolute accuracy of 10^{-4} of full scale. The accurate (0.002 °C), high-resolution (0.0001 °C) temperature sensor and internal temperature compensation ensure a residual temperature sensitivity in pressure data <3.5 N m^{-2} °C^{-1} in the range between 0 and 20 °C. The bottom-pressure

Latitude	30°00.052′N
Longitude	28°18.802′W
Water depth	549 m
Local bottom slope	4 ± 1°
Moored period	21/05–08/06 2006
Pressure sensor	SBE53, 0.33 Hz, 1.70 m above the bottom
Current meter	Nortek AquaDopp, 0.2 Hz, 2.50 m above the bottom
Acoustic Doppler current profiler	RDI 300 kHz, 0.53 Hz, lowest bin 4 m above the bottom, $80 \times \Delta z = 1$ m
Thermistor string	NIOZ3, 1 Hz, lowest sensor 0.5 m above the bottom, $101 \times \Delta z = 0.5$ m
Current speed	0–0.5 m s^{-1}
N, N_{1max}	50, 600 cpd (cycles per day)

TABLE 1. Details of bottom-lander mooring near the top of Great Meteor Seamount.

sensor has an absolute accuracy of $\sim$20 N m^{-2} and a resolution of 3 N m^{-2} for the 0.33 Hz sampling rate. These values are adequate to measure $O(10\text{–}10^2)$ N m^{-2} non-hydrostatic and internal hydrostatic pressure variations induced by, for example, internal waves, which, moreover, are found at much lower frequencies than the sampling frequency of 0.33 Hz. For small-scale internal waves near the buoyancy period of 600 s, random sampling errors are <4 N m^{-2}.

From tilt-sensor information it is inferred that the 200 kg bottom lander vibrates slightly under strong turbulence. This causes very high-frequency (>0.1 Hz) pressure variations (‘noise’) up to 10 N m^{-2}. These vibrations do not influence the pressure observation of the relevant processes, as no significant coherence has been found between tilt and pressure variations (see further § 4).

In addition to the pressure sensor, a Teledyne RDI 300 kHz acoustic Doppler current profiler (ADCP), sampling at a rate of 0.5 Hz, and a 1.5 MHz single-point acoustic current meter (Nortek AquaDopp), sampling at 0.2 Hz, are mounted in the lander. The closest current measurement to the sea floor was by the AquaDopp, at 2.5 m above the bottom. The ADCP ranged from 4 to $\sim$50 m above the bottom. It only rarely reached to its maximum range of 85 m above the bottom when sufficient acoustic scatterers were floating by. A string of 100 NIOZ high-sampling-rate thermistors (van Haren *et al.* 2009) measured temperature precisely (<0.001 °C) at 1 Hz and at 0.5 m vertical intervals between 0.5 and 50 m above the bottom. Directly above the string another 0.2 Hz sampling AquaDopp was mounted just below the top buoy.

Although instrumentation and mounting should be adequate to resolve internal wave turbulence pressure variations, estimates of the pressure terms in (2.1), (2.3), (2.4) or (2.5) all have some shortcomings. Precise knowledge of instrumental qualities is necessary prior to analysing the observations. ADCP data are relatively noisy due to a general lack of scatterers and reflections off thermistors in the observational area. These reflections are easily identifiable, but reduce the number of good data. More generally, current data are only obtained in the range [2.5, 80] m above the bottom in nearly 550 m water depth. Thus we lack data very close to the bottom, which somewhat hampers estimate (2.4), and we lack surface current data and hence estimates of p_{eh}, although they are expected to be small. The ADCP uses four slanted beams and gives current estimates over horizontal surface areas with diameters between 10 and 60 m, which approximate the smallest wave scales, thereby underestimating their current values in estimates like p_{nh} (Moum & Smyth 2006).

Even though we only resolve about 10 % of the water column, the present data set is not as limiting as it seems because most significant contributions to bottom pressure are expected from motions close to the bottom (Thomas & Bull 1983), except for hydrostatic surface tides. Following the reasonable assumptions for internal wave pressure terms made in Moum & Smyth (2006), one can state that: (i) for linear but also smoothly varying nonlinear waves, advection terms contribute <10 % to $\mathrm{D}w/\mathrm{D}t$, so that local time derivatives can be used to estimate p_{nh}, at least for $z > 10$ m above the bottom, which is resolved here; (ii) the lack of p_{eh} estimates will not alter the bottom-pressure effects of near-bottom solibore elevation wave types, which are barely noticeable at the surface 550 m above; and (iii) part of the investigation here includes a comparison between p_{ih} and p_{nh} estimates with p_{obs}^{-H}. This investigation will include the effects of near-bottom nonlinear and overturning waves and their extent into the water column up to 50 m above the bottom. It is hypothesized that p_{nh} may be more affected than p_{ih} by a lack of observations higher up in the water column, since the vertical extent of stratified thin layers can be much smaller than that of their associated vertical motions even though the range of their coherency is the same (e.g. van Haren 2009).

4. Observations

4.1. *General overview observations*

Above the sloping side of GMS, a total near-bottom temperature record shows a dominant semidiurnal tidal cycle and its spring–neap modulation (figure 2*a*, purple). In more detail, the temperature variations with time are not sinusoidal in shape, but more asymmetric. Removal of tidal harmonics and lower-frequency variations reveals the sharp nonlinear part of the asymmetric motions (figure 2*a*, black). Once every tidal cycle a major front passes the sensors. The front leads the upslope cooling tidal phase, but the strength of the front and its precise arrival time at a fixed position vary by up to ~10 % every tidal cycle. They are thus not modulated by spring–neap variation and the same holds for occasional secondary fronts following a few hours later. In addition, less spiked and smaller high-frequency variations are more persistent throughout the record, with largest amplitudes mostly in the down-going warming tidal phase just prior to the arrival of the major front.

In comparison, the observed total near-bottom pressure record shows a similar spring–neap modulated semidiurnal tidal dominance (maximum 0.9 m range), mainly dominated by the surface barotropic tide, and more sinusoidal in appearance (figure 2*b*, purple) than T variations. In contrast, the pressure part without tidal harmonics and lower-frequency variations, after using double elliptic band-pass filters (figure 2*b*, black; see figure 3 for filter bounds) is more continuously noise-like in time than its temperature equivalent. This featureless high-pass filtered pressure record p' shows only a weak fortnightly modulation about 5 days out of phase with the modulation in the surface tide. The amplitudes of p' are maximum 100 N m^{-2}, more commonly several tens of newtons per square metre.

If we further separate into three parts this tidally filtered bottom pressure, we find tidal (but not spring–neap) variation and peaked changes of variance with time in its lower-frequency portion (figure 2*c*, light blue). The number of spikes roughly equals that in T' (figure 2*a*), but they occur at different times. This lower-frequency portion is the IWC band, in which the observed pressure spectrum falls off in frequency at a rate of $\log(p_{IWC}) = c - (2.0 \pm 0.3) \log(\sigma)$, with c a constant (figure 3, blue). It lies between

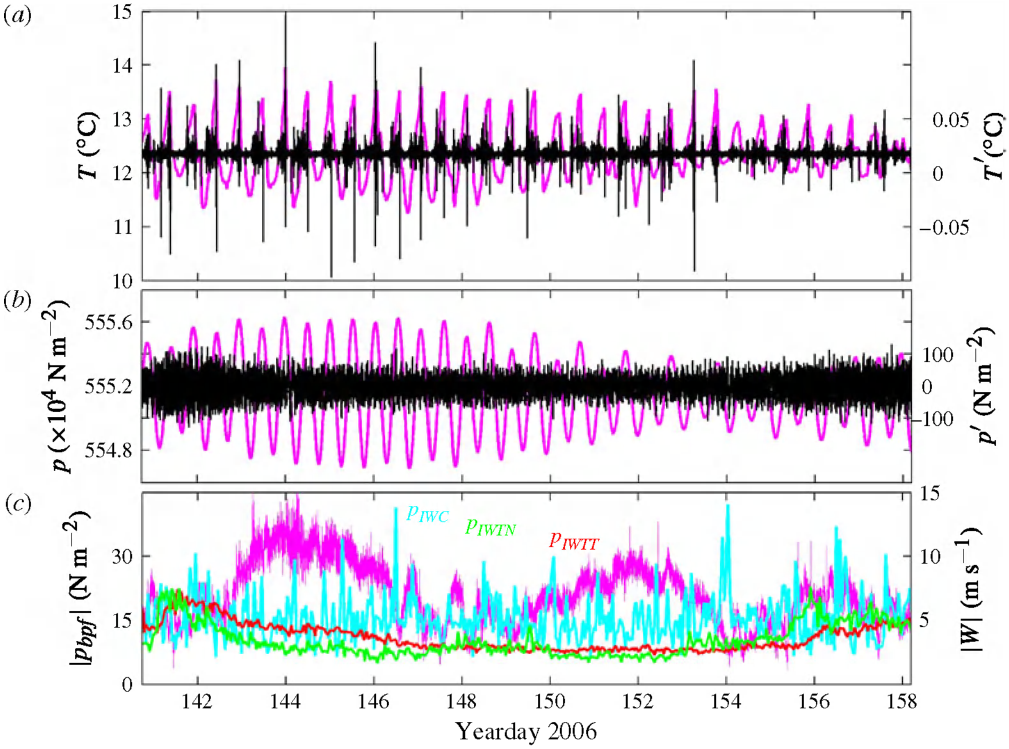

FIGURE 2. Overview of two-and-a-half weeks of time series data. (*a*) Near-bottom total temperature at 1.7 m above the bottom (purple), and its high-pass filtered variations (black; frequencies $\sigma > 7$ cpd; amplitude multiplied by a factor of 20; scale to right, and arbitrarily offset vertically). (*b*) As panel (*a*), but for pressure. (*c*) One-hour averaged, band-pass filtered (cf. figure 3 for filter bounds) near-bottom pressure amplitudes: $|p_{IWC}|$ (light blue), $|p_{IWTN}|$ (green), and $|p_{IWTT}|$ (red). Also shown is wind speed (purple; scale to right) measured every 60 s on board R/V *Pelagia* and corrected for the ship's speed.

tidal harmonics and the band containing the internal wave transition to turbulence IWT.

Although acceleration spectra (figure 3, purple), estimated using ADCP tilt sensor data, show approximately the same slope as observed bottom pressure in the IWC band, their variance is two orders of magnitude smaller. In the very high-frequency notch of bottom pressure ($\sim 6 \times 10^3$ cpd), the two spectra match in variance. This is evidence only in that frequency range of some influence of lander movements on the bottom-pressure observations (by limiting the depth of the notch).

The above IWC bounds do not coincide with the classic IW bounds under the traditional approximation $[f, N], = [1, 50]$ cpd here. At the low-frequency side, this is due to the contribution of tidal harmonics to bottom pressure and to weakly stratified near-homogeneous layers forcing N to approach f occasionally. At the high-frequency side, it is due to small-scale layering in density. The 90th percentile value of buoyancy frequency computed over small vertical scales of $\Delta z = 1$ m is set to N_1. It coincides with the kink in spectral slopes that indicates the transition between IWC and IWT. The N value calculated over $\Delta z = 1$ m varies over two frequency decades, a broad band that thus easily covers the spectral IWC range.

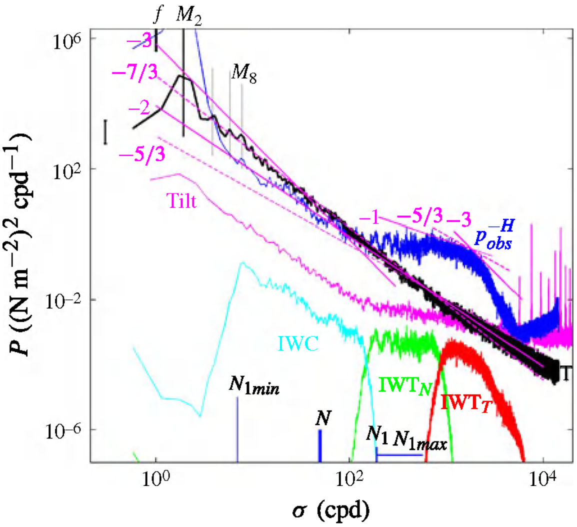

FIGURE 3. Spectra of observed near-bottom pressure (blue) in comparison with near-bottom temperature (black; arbitrarily offset vertically) and its pass-band filter bounds (same colours as in figure 2c; offset vertically). Also shown is the vertical acceleration inferred from ADCP's tilt data in units of pressure (purple). Several buoyancy frequencies are indicated: $\Delta z = 1$ m minimum, mean, 90th percentile of 1 m, and 1 m maximum, by blue bars in descending order. Spectral slopes are given (purple), which may mimic internal waves (σ^{-2}, solid), stratified turbulence (σ^{-3}, solid, repeated in IWT$_T$ range), inertial (turbulent) convective subrange ($\sigma^{-5/3}$, dashed, repeated in IWT$_T$ range) and low-wavenumber pressure turbulence transferred to frequency range (Gotoh & Fukayama 2001) ($\sigma^{-7/3}$, dashed).

The value of N_1 is found to extend well into IWT (figure 3); 10 % of the high-frequency 'internal wave' thin-layer buoyancy frequencies are found in this range. Here, we use the extreme N_{1max} to separate this band at the non-significant maximum of the IWT bulge into a 'buoyancy frequency internal wave/turbulence part' IWT$_N$ and a pure 'turbulence' part IWT$_T$. This separation frequency also coincides with the transition of the near-bottom T spectrum (figure 3, black) from a $\sigma^{-7/3}$ slope to a $\sigma^{-5/3}$ slope, when we ignore the statistical significance and when we take into account that spectra are plotted logarithmically so that we should give more emphasis to higher than to lower (neighbouring) values. (Compared to χ^2 noise distribution of statistical significance, most of the T spectrum, excluding tidal harmonics, lies within a -2 ± 0.3 fall-off rate.) A $-5/3$ slope is commonly attributed to high-wavenumber 'Kolmogorov' turbulence scaling, a $-7/3$ slope to low-wavenumber inertial range turbulence, but so far for simulated 'theoretical' pressure mainly (Gotoh & Fukayama 2001; Tsuji & Ishihara 2003), rather than for temperature and in a different frequency range than observed here.

In contrast to the T spectrum, the p spectral slope in the IWC band $\log(p_{IWC}) \approx -2 \pm 0.1$, which confirms the notion that internal waves dominate the inertial turbulence range in p_{obs}^{-H}. At frequencies higher than those of the IWC, the flat bulge maximum part of the p spectrum and especially its -1 and more steeply sloping high-frequency roll-off rate for $\sigma > N_{1max}$ is dominated by turbulence. This is provisionally concluded from its similarity with high-Reynolds-number free stream turbulence p spectra that roll off from a flat bulge at rates between -1.0 and -1.6 before steeper

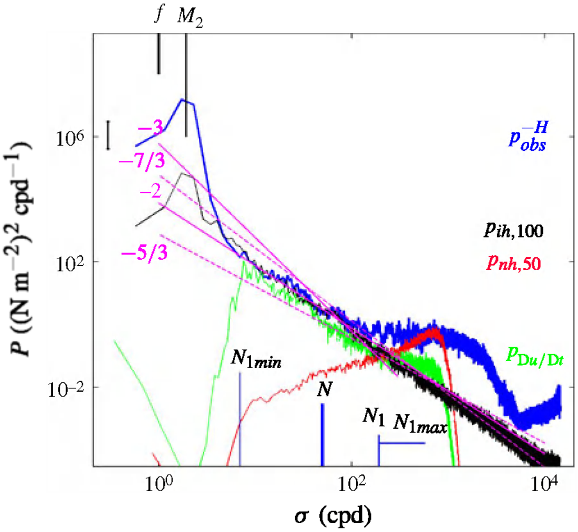

FIGURE 4. Spectra of observed near-bottom pressure (blue, same as in figure 3, given here for reference) in comparison with several internal wave pressure estimates following (2.1) and (2.3): p_{nh} (red, cut-off at border $\mathrm{IWT}_N/\mathrm{IWT}_T \sim N_{1max}$) inferred from AquaDopp's near-bottom vertical current, which are verified to be comparable with ADCP data from two depths, and assumed to be valid for a 50 m vertical range; p_{ih} (black) inferred from NIOZ thermistor string temperature data. Bottom pressure is also estimated from AquaDopp near-bottom horizontal current data $p_{\mathrm{D}u/\mathrm{D}t}$ (green, using constant $c = 0.5$ m s^{-1}, same cut-off as p_{nh}). See text for definitions and precise calculations. Slopes as in figure 3.

roll-off (Willmarth 1975; Tsuji *et al.* 2007). Turbulence may be associated with the dominant tidal motions (see also discussion in § 5), thereby partially explaining the fortnightly modulation in IWT (figure 2*c*), but surface infra-gravity waves above deep water far from coasts are unlikely to be so. Variance in none of the three band-pass filtered pressure parts is significantly coherent with the local wind speed (figure 2*c*, purple), which predominantly shows a diurnal and a 6-day periodicity. Occasionally, IWC and IWT_N modulations match over a short period with $|W|$ and generally not together at the same time, and their mutual correlation is found to be insignificant over the entire period of 18 days.

The difference in the spectral slopes of temperature and pressure is attributable to their different measurement: pressure acts like an integrator of the (wave) motions above it. This difference is independently demonstrated by integrating temperature over the full 50 m above the bottom of the thermistor observations. This results in an (internal wave) estimate of p_{ih}. When transferring temperature to density variations and assuming that they represent the lower 100 m of the water column commensurate with the typical internal (tidal) wave vertical coherence scales and the extent of associated turbulent overturns (van Haren & Gostiaux 2012*a*), one finds (figure 4, black) the σ^{-2} slope and a near-perfect match. This is well within the statistical 95 % significance bounds, with p_{obs}^{-H} in the IWC (between N_{1min} and N_1).

The same IWC slope and approximately the same level, although slightly less in variance by about 30 %, which is still larger by a factor of 2 than the reduction found by Moum & Smyth (2006), is independently obtained from the pressure estimate (2.3), $p_{\mathrm{D}u/\mathrm{D}t}$ component, using AquaDopp's along-slope currents at 2.5 m above the bottom and assuming a constant phase speed (figure 4, green). This spectrum changes slope towards instrumental noise approximately at N_1.

For $\sigma > N_1$, lower-frequency dominant p_{ih} becomes overwhelmed by p_{nh} (figure 4, red), which is estimated here from AquaDopp's near-bottom vertical motions as a representative of the range of thermistor observations. (This is probably an overestimate, because of the instrumental noise in w, especially in the range for IWT$_T$. This noise is thus largely filtered out here. In § 4.2 we estimate p_{nh} using ADCP data, which are only good over short sections of time but not over the entire record at every depth.)

For the two-week mean in figure 4 we thus conclude that observed bottom pressure is dominated by p_{ih} in the IWC ($R_{p,-H} \ll 1$; from (2.2)) and by p_{nh} and turbulent stress in the IWT ($R_{p,-H} \gg 1$). Below, the contributions of the different terms are investigated for some periods in detail. Owing to the shortness of these periods, we focus on motions near the local buoyancy frequency or highly nonlinear waves. These motions will thus be mainly non-hydrostatic ($R_{p,-H} \gg 1$) and potentially $R_{p,-H} = 1$ for freely propagating internal waves near the small-scale buoyancy frequency N_1, which indicates the transition between p_{ih} and p_{nh} dominance (figure 4).

4.2. *Detailed observations*

The passage of an upslope frontal bore (figure 5; 0.6 h detail) is accompanied, shortly before and after, by strong downward and upward vertical motions exceeding 0.1 m s^{-1} (figure 5*a*) and by a single very strong (40 dB above ambient level) echo moving upwards from the bottom (figure 5*b*). These observables are associated with sediment resuspension extending over 40 m above the bottom within minutes. The front, delineating the highly nonlinear end of the downslope moving tidal warming phase, is trailed by a series of 'free' waves having about the local buoyancy period. The trailing waves are supported by the thin-layer stratification between the warm downslope moving water above and colder upslope moving water below (figure 5*c*). Such a strong bore occurs here approximately once every sloshing tidal cycle, but similar bores, one including 24 h run-up, have been reported governed by sloshing sub-inertial current systems in other areas (Hosegood & van Haren 2004; Grue & Sveen 2010).

Although the trailing high-frequency waves characterized by typical 600–900 s periods and 10–20 m amplitudes are discernible in bottom pressure and more clearly in temperature (figure 5*c*), the detailed temperature image is dominated by rugged quasi-turbulent motions. Such turbulent motions are not only observed around the (curved) front, but also scattered around the image in small details. The apparent 'periods' of these turbulent motions are far shorter than the smallest buoyancy period computed ($2\pi/N_{1max} \sim 150$ s), as they reach down to periods $O(10$ s$)$.

Such short-period variability is dominant in the high-frequency bottom-pressure record (figure 5*c*, purple; arbitrary scale), and it can be more or less matched with variations in the temperature image in the same figure. This variability is so omnipresent that the frontal bore does not stand out very clearly in p^{-H}_{obs}. A dip of about -50 N m^{-2} is measured at the time of the bore's passage (more clearly visible in figure 5*e*, purple; the same record as in figure 5*c*), but many such dips or spikes occur in the record. From a bottom pressure perspective the frontal bore is not an exceptional phenomenon.

The bore is more clearly visible in the separate estimates of (internal wave) bottom pressure: all show a dip (figure 5*e*, blue $p_{\mathrm{D}v/\mathrm{D}t}$ that matches very well the dip in purple p^{-H}_{obs}) or a front (figure 5*d*,*e*, red p_{nh}, black p_{ih}, green $p_{\mathrm{D}u/\mathrm{D}t}$) of 20–50 N m^{-2}

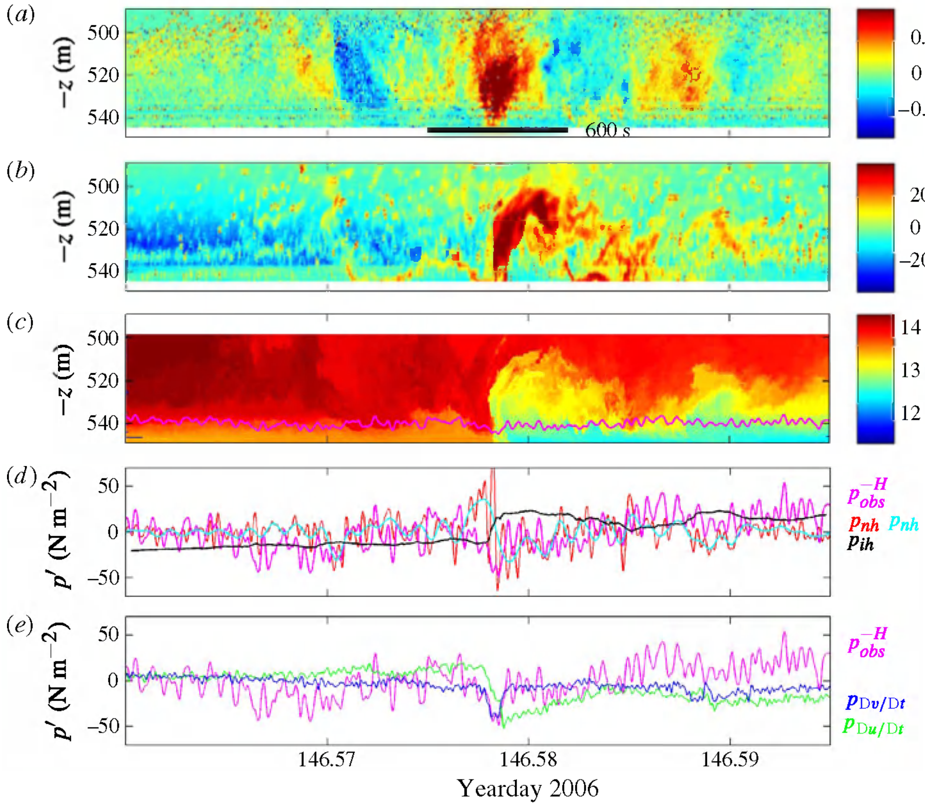

FIGURE 5. Example of relatively large IWC contributions to bottom pressure and a large, backwards breaking, upslope moving bore and its trail in a 0.6 h detail. (*a*) Depth–time series of ADCP's raw vertical motions. The horizontal lining in the lower half of the figure and the noise speckles higher up are due to artificial reflectance off T sensors. (*b*) ADCP's relative echo intensity. See remark about panel (*a*) on the influence of thermistors on acoustic data. (*c*) Temperature measured at 1 Hz, 0.5 m vertical intervals. The bottom-pressure record (purple) $\mathrm{IWC}+\mathrm{IWT}_N+\mathrm{IWT}_T$ band-pass filtered is also shown (arbitrary scale). (*d*) The band-pass filtered observed bottom pressure (purple) $\mathrm{IWC}+\mathrm{IWT}_N+\mathrm{IWT}_T$ plotted with p_{nh} (red) and p_{ih} (black) estimated over the range of thermistors, and with $\mathrm{IWC}+\mathrm{IWT}_N$ band-pass filtered p_{nh} (light blue). (*e*) The band-pass filtered observed bottom pressure (purple) $\mathrm{IWC}+\mathrm{IWT}_N+\mathrm{IWT}_T$ compared with independent near-bottom (1.7 m above the bottom) pressure estimates of cross-slope $p_{\mathrm{D}v/\mathrm{D}t}$ (purple) and along-slope $p_{\mathrm{D}u/\mathrm{D}t}$ (green) using a constant $c = 0.2$ in (2.3).

in amplitude around the bore's passage. As already noted in their spectra, p_{nh} and p_{ih} have approximately the same range of variation but a completely different character: p_{nh} is dominated by higher-frequency variations compared to p_{ih}. Around the bore's passage, their signs are commensurate with those for elevation waves (Moum & Smyth 2006): they are opposite in sign and roughly cancel each other out here for motions at $\sigma \approx N_1$. Note that in this case p_{nh} is computed from integrating the ADCP's vertical motions (figure 5*a*) approximately over the same range as the thermistors, except for the lower 4 m (no ADCP data) and upper 5 m of the thermistors' range (some lack of scatterers for ADCP). The exclusively upslope movement of the frontal bore is well retrieved, as the dips in the $p_{\mathrm{D}v/\mathrm{D}t}$ term and observed bottom pressure are nearly indistinguishable (figure 5*e*).

Also, around the time of the bore's passage, including the first large overturn on day 146.5785, p_{nh} shows more variance than in the rest of the tidal period. The front marks a transition from smooth (low-frequency IWC variance dominated) to slightly more noisy (high-frequency IWC increased) p_{ih} (figure 5*d*). Away in time from the bore's passage, after day 146.61, the slower (IWC) variations in p_{obs}^{-H} (purple) are not so well mimicked by the independent estimates of pressure terms (not shown). Apparently, variations higher up in the water column are more important in this example when stratification moves out of the range of the sensors, especially in p_{ih}. Although exact phase correspondence is lacking, the intensity (amplitude and variation with time) of higher-frequency IWT motions is comparable in p_{nh} (red) and p_{obs}^{-H} (purple) (figure 5*d*).

The independent estimate $p_{\mathrm{D}v/\mathrm{D}t}$ (figure 5*e*, blue) shows marginal IWT variations, and generally fails to describe the IWC as in p_{obs}^{-H} (purple). An exception is around the time of the bore passage, when motion is strictly up the slope. This lack of comparison for IWC is partially compensated in $p_{\mathrm{D}u/\mathrm{D}t}$ (green) further in the record, which better follows typical IWC 600–900 s periodic variations, but not entirely because near-bottom currents are just not well measured, not even by the AquaDopp at 2.5 m above the bottom. So, while high-frequency IWC and low-frequency IWT, i.e. motions at $\sigma \approx N_1$, including a frontal passage, are comparable in size for p_{nh} and p_{ih} with opposite signs, the exclusively upslope moving front is best observed in $p_{\mathrm{D}v/\mathrm{D}t}$ with a near-perfect match with p_{obs}^{-H} (figure 5*e*). In contrast, $p_{\mathrm{D}u/\mathrm{D}t}$(figure 5*e*, green) describes p_{nh} (IWC + IWT$_N$ part; figure 5*d*, light blue). As noted from the spectra, turbulence dominates (the IWT part of) p_{obs}^{-H} and it is recalled that the estimates (2.1) and (2.3) are for waves.

The lack of bottom current measurements is somewhat more problematic during a period prior to a bore arrival, when stratification reaches very close to the bottom and low amounts of scatterers are found higher up (figure 6; 1 h detail). This period seems to be dominated by high-frequency local apparent vertical mode-2 internal 'motions' close to the local buoyancy period of ~450 s (figure 6*c*). Vertical currents are weak, indicative of a lack of large vertical coherence, and the stratification is mainly moved by quasi-turbulent motions. As before, p_{nh} (figure 6*d*, red) mimics well the observed bottom pressure (purple) in IWT variance, whereas here weak p_{ih} (figure 6*d*, black) is only marginally retrieved in p_{obs}^{-H} (purple). The $p_{\mathrm{D}v/\mathrm{D}t}$ (figure 6*e*, blue) and $p_{\mathrm{D}u/\mathrm{D}t}$ (figure 6*e*, green) mainly describe IWC rather than IWT, with a reasonable comparison between $p_{\mathrm{D}u/\mathrm{D}t}$ and observed IWC pressure in the second half of the period. Observed IWT pressure variations are visible in both $p_{-H,obs}$ and short-term 'turbulent' temperature variations (figure 6*c*). These variations thus do not reflect direct surface wave variations, as even the small-scale turbulent overturning temperature interface variations have amplitudes of several metres in the vertical, rather than $O(10^{-3}\ \mathrm{m}) \cong O(10\ \mathrm{N\ m^{-2}})$ for IGW surface waves.

In an arbitrary, more detailed zoom (figure 7), near-buoyancy frequency internal waves of 500 s period (figure 7*a*) support the shorter (down to 20 s) period motions, also away from the interface that carries them (local maximum buoyancy period in the interface equals 450 s). In the weaker stratified layer, these 'waves' do not lose coherency completely, amid the overturns, even though the local stratification does not support them as freely propagating waves. At the interface and also away from it, 20–50 s period motions occur often, albeit intermittently in time, having typical 0.5–1 m amplitudes (more clearly visible in detail in figure 7*b*,*d*). The dominant periodicity in p_{obs}^{-H} (purple) is 20–50 s, and it compares with isotherm variation

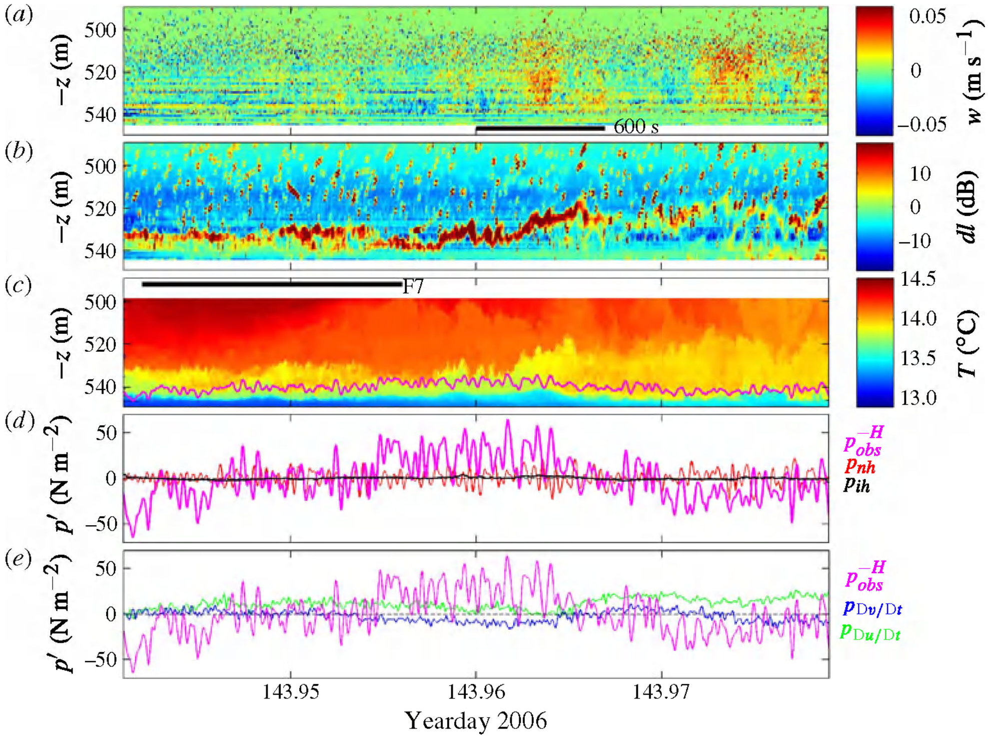

FIGURE 6. As figure 5, but for 1 h mainly typifying a moderately turbulent, downslope tidal phase before the arrival of an upslope bore. This zoom period is characterized by large high-frequency p_{nh} and small p_{ih} variability. Note the difference in some colour scales compared to figure 5. In panel (*a*), lack of scatterers causes poor current data resolution above 510 m. The bar in panel (*c*) denotes the time range of figure 7. In panels (*c*) and (*d*) bottom pressure data/estimates are IWC + IWT$_N$ + IWT$_T$ band-pass filtered.

with time, notably in figure 7(*d*). Note, however, the rapid changes in isotherm displacements relative to the isotherm at ~4 m above the bottom. The 20–50 s turbulence 'periodicity' is also dominant in p_{nh} (figure 7*c*, red), which thus reflects associated vertical motions. However, its phase correspondence with p_{obs}^{-H} obviously remains ambiguous and depends on different sampling strategies. Some sampling effects are already visible in a small test comparison between p_{nh} following integration over 25 m (figure 7*c*,*e*, light blue), 45 m (figure 7*c*,*e*, red, standard range) and 80 m (figure 7*c*,*e*, blue).

5. Discussion

A typical description of the seismic noisy (deep) ocean bottom-pressure spectrum like that in figure 3 (e.g. Filloux 1980; Webb 1998) attributes the nearly flat, wide bulge between frequencies $10^2 < \sigma < 2 \times 10^3$ cpd to long surface waves, IGW, such as tsunami waves and waves that result from nonlinear interaction between shorter wind waves. Such waves are weakly attenuated, and can thus propagate across an entire ocean (e.g. Bromirski, Sergienko & MacAyeal 2010). As a result, they may not be related to local atmospheric variations, except perhaps in relatively small enclosed seas. Their tracing may involve knowledge about disturbances in far away areas.

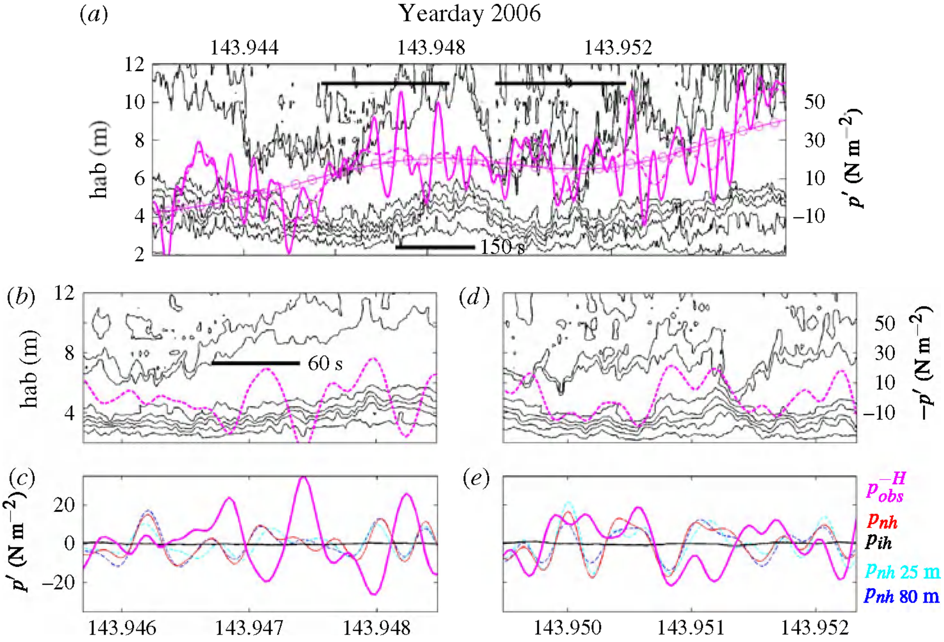

FIGURE 7. Near-bottom 1200 s detail of figure 6, highlighting 17–50 s time scale turbulent 'wave-like motions'. (*a*) Temperature contours between [13.3, 14.0] °C in 0.1 °C intervals. Also shown is the bottom-pressure record (purple), differently band-pass filtered (IWC + IWT_N + IWT_T, solid; IWC + IWT_N, dash-dotted; IWC, line with circles); scale to right. Bars indicate 250 s detail panels to left (*b*,*c*) and right (*d*,*e*) columns. (*b*) Detail of panel (*a*), in which (inverse) IWC + IWT_N + IWT_T bottom pressure does not well match the temperature contour variations. (*c*) Bottom pressure as in panel (*a*) (purple), compared with three estimates of p_{nh} (red, as before; and light blue, blue for height ranges above the bottom as indicated) and p_{ih} (black, multiplied by a factor of 10 as if governed by the entire water column). (*d*,*e*) As panels (*b*,*c*), but for period in which (inverse) bottom pressure partially matches temperature contour variations.

Nonetheless, for a number of reasons, such surface waves cannot force turbulence above sloping topography as observed here, even though the dominant bottom-pressure variations fall within the same frequency range. First, the fortnightly spring–neap modulation as observed here is not a result of an interaction between distant 'storm-modulated' surface waves (van Haren 2011). Even though tidal (high and low water) modulation of surface infra-gravity waves has been reported for shallow waters close to shore (Okihiro & Guza 1995), this cannot cause a dominant spring–neap modulation out in the open ocean, where waves from multiple shores with different tidal phases combine. Second, one cannot dismiss the energy input of internal tides, into higher harmonics and into eventual strongly nonlinear motions, without neglecting the transition to turbulence as in overturning motions observed here. (It is noted that some nonlinear regimes exist in which the motion is not turbulent (Grue 2005).) Third, surface IGWs do not create the observed highly nonlinear frontal bore, which is density-driven, nor Kelvin–Helmholtz overturning, which is shear-driven. The latter occur in the downslope phase and have a 20–50 s periodicity, which is far smaller than the smallest internal wave period (van Haren & Gostiaux 2010). Fourth, if surface IGWs would create 'turbulence' IWT, they should also do so in the ocean interior, not exclusively above sloping topography. This is not observed in similar detailed temperature observations far from boundaries in the Canary Basin, which show weakly turbulent, smooth internal waves (van Haren & Gostiaux 2009).

Recent estimates of turbulence parameters have been made for the dynamic GMS sloping boundary by means of reordering all of the 1 Hz sampled temperature-sensor profiles using the method proposed by Thorpe (1977). These estimates yield highly varying turbulence dissipation rates between $10^{-9} < \varepsilon < 10^{-4}$ W kg^{-1}, with a depth–time mean of $\langle\varepsilon\rangle = (1.5 \pm 0.7) \times 10^{-7}$ W kg^{-1} (van Haren & Gostiaux 2012*a*). The variance of depth-averaged dissipation rates has been compared with the variance of various pressure terms, which resulted in a coherent signal, with 180° phase difference, at 75 % significance level at semidiurnal and its first harmonic frequencies. Van Haren & Gostiaux (2012*a*) demonstrate that the spectrum of heat flux transits from the canonical internal wave -2 slope to the turbulence $-5/3$ slope at the frequency where the eddy diffusivity and the pressure spectra transit from their IWC slope to the IWT bulge. Furthermore, the spectral shape of variance and particular time series of intermittent turbulence pressure and vertical currents resemble turbulence observations in the atmospheric boundary layer. The present observed lack of precise phase correlations does not imply a lack of correspondence between source (internal waves) and turbulence dissipation as was intrinsically proven for measurements in the turbulent atmospheric boundary layer (Cuxart *et al.* 2002). The different wave pressure terms p_{ih} (IWC mainly) and p_{nh} (IWT mainly) show spectral shapes and variances in their respective frequency bands that are comparable with those of p_{obs}^{-H}. It implies that the vertical length scale of integration (50–100 m above the bottom) is adequate, in most instances, especially for estimating p_{nh}. A future more complete data set should establish this more firmly.

The spectral shape of IWC, being self-similar in constant slope and variance (Filloux 1980; van Haren 2011), thus representing a saturated internal wave field, and IWT, with a varying bulge variance, are consistent with the internal wave turbulence model of D'Asaro & Lien (2000*a*,*b*). This model resembles the neutral atmospheric law-of-the-wall turbulence pressure spectrum (Willmarth 1975). However, we note that the present turbulence is partially generated in the interior, occasionally resulting in a turbulent bore moving up a sloping bottom, with relevance for sediment resuspension.

This difference in turbulence character is evidenced in a consistency test for law-of-the-wall turbulence, using 10 min intervals of figure 5. We fit ADCP velocity profiles with the model of a constant (bottom frictional shear) stress layer to obtain a friction velocity u_* (Wyngaard 1973)

$$u(z) \propto \frac{u_*}{\kappa} \ln z, \tag{5.1}$$

with $\kappa = 0.4$ denoting the von Kármán constant. Independently, u_* is estimated using the above high-resolution thermistor string data. It is estimated under the rather crude assumption of negligible buoyancy flux, so that the kinetic energy production matches the dissipation rate ε,

$$u_*^3 = \varepsilon \kappa z. \tag{5.2}$$

Although the two different estimates are found to be consistent to within a factor of 3, the law-of-the-wall model overestimates the friction velocity before and after the front, and underestimates it during the frontal passage (figure 8). It is clear that a tight logarithmic profile is not observed. Also, a two-fold log layer ('modified law of the wall'), as in Perlin *et al.* (2005), is not observed here. These discrepancies with

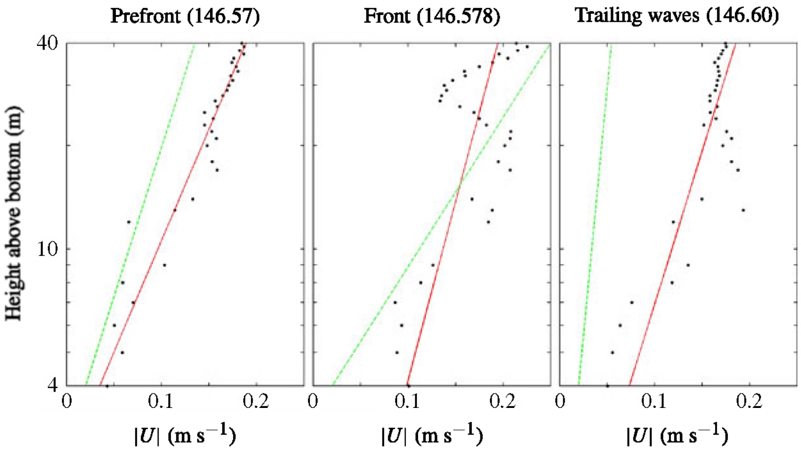

FIGURE 8. Law-of-the-wall turbulence test for three 10 min periods around the frontal passage of figure 5. Dots indicate the ADCP-observed current magnitudes (with low biased values due to reflection at thermistors removed). The red line is the log-linear best fit to these data to provide a friction velocity following (5.1). The green dashed lines indicate hypothetical slopes (using arbitrary initial depths) for friction velocities independently computed using (5.2) for $z = 10$ m from turbulence dissipation rates estimated using high-resolution thermistor string data (van Haren & Gostiaux 2012*a*).

models (5.1) and (5.2) may have to do with the boundary layer above a sloping bottom being nearly always (re)stratified in density (figure 5) so that turbulence isotropy may not be achieved, except perhaps very briefly during the passage of a turbulent bore.

A similar result is obtained after comparison of the turbulent part of the observed bottom pressure, p_{IWTT}, with pressure independently estimated from dissipation rates using high-resolution temperature data between 0.5 and 50 m above the bottom (for the method, see van Haren & Gostiaux (2012*a*)). Under the assumption of isotropic turbulence and high-Reynolds-number flows, Kolmogorov scaling yields at wavenumber k for the, presumably free stream rather than bottom or wall, pressure spectrum (Tsuji & Ishihara 2003)

$$P_p(k) \propto p_\varepsilon^2 = K_p \rho^2 \varepsilon^{4/3} k^{\gamma_p}, \quad \gamma_p = -7/3, \tag{5.3}$$

in which K_p denotes a 'universal constant'. Extensive (free stream pressure) laboratory observations were made by Tsuji & Ishihara (2003) up to Reynolds number $Re = UL/\nu = 15\,000$, with kinematic viscosity $\nu \approx 1.5 \times 10^{-6}$ m^2 s^{-1}, and U and L the velocity and length scales of the flow. Their results yielded higher γ_p and smaller exponent of ε than in (5.3). They also found a linear dependence of $K_p \propto Re/150$ and they attributed their findings to non-isotropic turbulence. Here, restratification occurs rapidly and continuously. As average $U = 0.2$ m s^{-1} and a typical $L = 0.1$–10 m, one has $Re \sim 10^4$–10^6, very large indeed. A fit of overall mean p_ε is made to mean p_{IWTT} (approximately mean p_{IWTN}) using both (5.3) and $\gamma_p = -4/3$ as the mean of exponents found by Tsuji & Ishihara (2003). In the fitting, $K_p(Re)$ and k (wavelength λ) are used as parameters, yielding best fits for the combinations $\lambda = 10$ m, $Re = 5 \times 10^6$ and 3×10^5, respectively, and $\lambda = 50$ m, $Re = 1.1 \times 10^5$ and 6×10^4, respectively. The Reynolds numbers are in the expected high range. In figure 9, the time series p_ε (blue) provides a similar spring–neap variation compared to those of p_{IWTT} (red) and p_{IWTN}

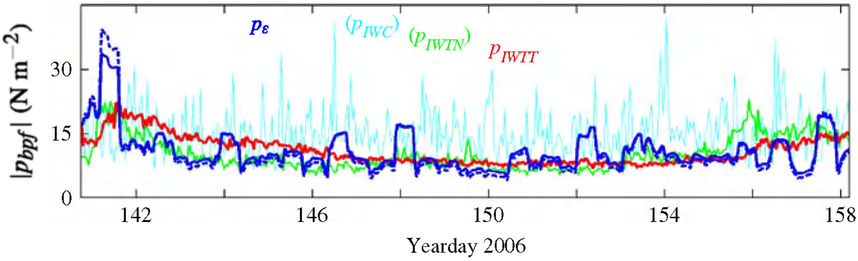

FIGURE 9. As figure 2(*c*) without wind speed and with 10 h smoothed pressure estimated from turbulence dissipation rate using high-resolution temperature data from 101 sensors between 0.5 and 50 m above the bottom. Two parametrizations are used: $p_\varepsilon^2 \propto \varepsilon^{4/3}$ (dashed blue) following (5.3) as in Kolmogorov scaling for isotropic turbulence in high-Reynolds-number flows; and $p_\varepsilon^2 \propto \varepsilon^{13/12}$ (solid blue, $\gamma_p = -4/3$) following the mean exponential value determined in laboratory turbulent flows (Tsuji *et al.* 2007). The empirical scaling values are given in the text.

(green). The p_ε has a more spiky character, and at times the comparison is better with the more variable time series of p_{IWTN} and even p_{IWC} (light blue) than p_{IWTT}. We do not expect an improved comparison between the mid-boundary layer (25 m above the bottom) p_ε and the observed bottom pressure, as ongoing restratification prevents turbulence from being isotropic.

So, some correspondence is found with wall turbulence, for which a pressure spectrum as in IWC and IWT here has been found for the atmosphere (Willmarth 1975). The 3 min bore passage comprises about 20 % of the total dissipation rate in a tidal period (van Haren & Gostiaux 2012*b*). However, turbulence is generated not only by shear stress at the bottom, but also by convection in the interior. The total amount of turbulence kinetic energy dissipated in the lower 50 m above the sloping bottom amounts to about a quarter of the total internal tidal energy conversion by Great Meteor Seamount (van Haren & Gostiaux 2012*b*). It remains to be established whether this is mainly due to (breaking) internal waves returning to their source.

6. Conclusions

Above a large-scale ocean bottom topography, the variance of observed bottom pressure is found to be equivalent to independent estimates of internal hydrostatic pressure due to freely propagating internal waves up to 100 m above the bottom at frequencies lower than the buoyancy frequency, and of non-hydrostatic pressure following internal wave (breaking) turbulence in the lower 50 m above the bottom at frequencies higher than the buoyancy frequency.

The internal wave turbulence non-hydrostatic pressure dominates over long surface wave bottom pressure, which may be found in the same frequency band.

Internal wave bottom pressure is also verified by near-bottom horizontal current (variations), in along-slope direction mainly, except during the passage of an upslope moving frontal bore that generates a clear dip.

The frontal pressure dip of only 50 N m^{-2} in directly observed bottom pressure is amid omnipresent, mainly non-hydrostatic, internal wave turbulence pressure, which is found to be weaker in independent (non)linear wave pressure estimates using near-bottom current observations.

As in the atmospheric turbulent boundary layer, precise phase relationships cannot be established between observed bottom pressure and different (internal wave) pressure estimates, especially not at frequencies higher than the buoyancy frequency.

As it shows no spectral gap, the transition between internal waves and turbulence is confirmed to be smooth.

Acknowledgements

I enjoyed the assistance of the crew of the R/V *Pelagia*. I am greatly indebted to M. Laan for construction of the NIOZ thermistors and to L. Gostiaux for facilitating thermistor data analysis. Instrumentation and research cruises were funded in part by the Netherlands Organization for the Advancement of Scientific Research, NWO (large investment program 'LOCO') and BSIK.

REFERENCES

AGHSAEE, P., BOEGMAN, L. & LAMB, K. G. 2010 Breaking of shoaling internal solitary waves. *J. Fluid Mech.* **659**, 289–317.

BONNIN, J., VAN HAREN, H., HOSEGOOD, P. & BRUMMER, G.-J. A. 2006 Burst resuspension of seabed material at the foot of the continental slope in the Rockall Channel. *Mar. Geol.* **226**, 167–184.

BROMIRSKI, P. D., SERGIENKO, O. V. & MACAYEAL, D. R. 2010 Transoceanic infragravity waves impacting Antarctic ice shelves. *Geophys. Res. Lett.* **37**, L02502.

CUXART, J., MORALES, G., TERRADALES, E. & YAGÜE, C. 2002 Study of coherent structures and estimation of the pressure transport terms for the nocturnal stable boundary layer. *Boundary-Layer Meteorol.* **105**, 305–328.

D'ASARO, E. A. & LIEN, R.-C. 2000*a* Lagrangian measurements of waves and turbulence in stratified flows. *J. Phys. Oceanogr.* **30**, 641–655.

D'ASARO, E. A. & LIEN, R.-C. 2000*b* The wave–turbulence transition for stratified flows. *J. Phys. Oceanogr.* **30**, 1669–1678.

FILLOUX, J. H. 1980 Pressure fluctuations on the open-ocean floor over a broad frequency range: new program and early results. *J. Phys. Oceanogr.* **10**, 1959–1971.

FRUCTUS, D., CARR, M., GRUE, J., JENSEN, A. & DAVIES, P. A. 2009 Shear-induced breaking of large internal solitary waves. *J. Fluid Mech.* **620**, 1–29.

GAYEN, B. & SARKAR, S. 2010 Turbulence during the generation of internal tide on a critical slope. *Phys. Rev. Lett.* **104**, 218502.

GERKEMA, T., ZIMMERMAN, J. T. F., MAAS, L. R. M. & VAN HAREN, H. 2008 Geophysical and astrophysical fluid dynamics beyond the traditional approximation. *Rev. Geophys.* **46**, RG2004.

GOTOH, T. & FUKAYAMA, D. 2001 Pressure spectrum in homogeneous turbulence. *Phys. Rev. Lett.* **86**, 3775–3778.

GRUE, J. 2005 Generation, ppropagation and breaking of internal solitary waves. *Chaos* **15**, 037110.

GRUE, J., JENSEN, A., RUSÅS, P.-O. & SVEEN, J. K. 2000 Breaking and broadening of internal solitary waves. *J. Fluid Mech.* **413**, 181–217.

GRUE, J. & SVEEN, J. K. 2010 A scaling law of internal run-up duration. *Ocean Dyn.* **60**, 993–1006.

HOSEGOOD, P. & VAN HAREN, H. 2004 Near-bed solibores over the continental slope in the Faeroe–Shetland Channel. *Deep-Sea Res.* II **51**, 2943–2971.

KLYMAK, J. M. & MOUM, J. N. 2003 Internal solitary waves of elevation advancing on a shoaling shelf. *Geophys. Res. Lett.* **30**, 2045.

LAMB, K. G. 2003 Shoaling solitary internal waves: on a criterion for the formation of waves with trapped cores. *J. Fluid Mech.* **478**, 81–100.

LAMB, K. G. & FARMER, D. 2011 Instabilities in an internal solitary-like wave on the Oregon shelf. *J. Phys. Oceanogr.* **41**, 67–87.

LEBLOND, P. H. & MYSAK, L. A. 1978 *Waves in the Ocean*. Elsevier.

MOUM, J. N. & SMYTH, W. D. 2006 The pressure disturbance of a nonlinear internal wave train. *J. Fluid Mech.* **558**, 153–177.

MOUM, J. N. & NASH, J. D. 2008 Seafloor pressure measurements of nonlinear internal waves. *J. Phys. Oceanogr.* **38**, 481–491.

OKIHIRO, M. & GUZA, R. T. 1995 Infragravity energy modulation by tides. *J. Geophys. Res.* **100**, 16 143–16 148.

PERLIN, A., MOUM, J. N., KLYMAK, J. M., LEVINE, M. D., BOYD, T. & KOSRO, M. H. 2005 A modified law-of-the-wall applied to oceanic boundary layers. *J. Geophys. Res.* **110**, C10S10.

PINKEL, R. 1981 Observations of the near-surface internal wavefield. *J. Phys. Oceanogr.* **11**, 1248–1257.

SHAW, R. H., PAW, K. T., ZHANG, X. J., GAO, W., DEN HARTOG, G. & NEUMANN, H. H. 1990 Retrieval of turbulent pressure fluctuations at the ground surface beneath a forest. *Boundary-Layer Meteorol.* **50**, 319–338.

SLINN, D. N. & RILEY, J. J. 1996 Turbulent mixing in the oceanic boundary layer caused by internal wave reflection from sloping terrain. *Dyn. Atmos. Oceans* **24**, 51–62.

SMITH, W. H. F. & SANDWELL, D. T. 1997 Global seafloor topography from satellite altimetry and ship depth soundings. *Science* **277**, 1957–1962.

THOMAS, A. S. W. & BULL, M. K. 1983 On the role of wall-pressure fluctuations in deterministic motions in the turbulent boundary layer. *J. Fluid Mech.* **128**, 283–322.

THORPE, S. A. 1977 Turbulence and mixing in a Scottish loch. *Phil. Trans. R. Soc. Lond.* A **286**, 125–181.

TSUJI, Y., FRANSSON, J. H. M., ALFREDSSON, P. H. & JOHANSSON, A. V. 2007 Pressure statistics and their scaling in high-Reynolds-number turbulent boundary layers. *J. Fluid Mech.* **585**, 1–40.

TSUJI, Y. & ISHIHARA, T. 2003 Similarity scaling of pressure fluctuation in turbulence. *Phys. Rev.* E **68**, 026309.

VAN HAREN, H. 2009 High-frequency vertical current observations in stratified seas and ocean. *Cont. Shelf Res.* **29**, 1251–1263.

VAN HAREN, H. 2011 Internal wave-turbulence pressure above sloping sea bottoms. *J. Geophys. Res* **116**, C12004.

VAN HAREN, H. & GOSTIAUX, L. 2009 High-resolution open-ocean temperature spectra. *J. Geophys. Res.* **114**, C05005.

VAN HAREN, H. & GOSTIAUX, L. 2010 A deep-ocean Kelvin–Helmholtz billow train. *Geophys. Res. Lett.* **37**, L03605.

VAN HAREN, H. & GOSTIAUX, L. 2012*a* Detailed internal wave mixing above a deep-ocean slope. *J. Mar. Res.* **70**, 179–197.

VAN HAREN, H. & GOSTIAUX, L. 2012*b* Energy release through internal wave breaking. *Oceanography* **25** (2), 124–131.

VAN HAREN, H., LAAN, M., BUIJSMAN, D.-J., GOSTIAUX, L., SMIT, M. G. & KEIJZER, E. 2009 NIOZ3: independent temperature sensors sampling yearlong data at a rate of 1 Hz. *IEEE J. Ocean. Engng* **34**, 315–322.

VENAYAGAMOORTHY, S. K. & FRINGER, O. B. 2007 On the formation and propagation of nonlinear internal boluses across a shelf break. *J. Fluid Mech.* **577**, 137–159.

VLASENKO, V. & HUTTER, K. 2002 Numerical experiments on the breaking of solitary internal waves over a slope-shelf topography. *J. Phys. Oceanogr.* **32**, 1779–1793.

WEBB, S. C. 1998 Broadband seismology and noise under the ocean. *Rev. Geophys.* **36**, 105–142.

WILLMARTH, W. W. 1975 Pressure fluctuations beneath turbulent boundary layers. *Annu. Rev. Fluid Mech.* **7**, 13–36.

WYNGAARD, J. C. 1973 On surface layer turbulence. In *Workshop on Micrometeorology* (ed. D. A. Haugen). pp. 101–149. AMS.

XING, J. & DAVIES, A. M. 2006 Processes influencing tidal mixing in the region of sills. *Geophys. Res. Lett* **33**, L04603.